photonics

MDPI

Communication

Dual Optical and Acoustic Negative Refraction in Phoxonic Crystals

Shuyi Zhao [1], Linlin Lei [1], Qin Tang [1], Feng Xin [2] and Tianbao Yu [1,*]

[1] School of Physics and Materials Science, Nanchang University, Nanchang 330031, China
[2] School of Mechanical and Electronic Engineering, Pingxiang University, Pingxiang 337000, China
* Correspondence: yutianbao@ncu.edu.cn

Abstract: We report dual optical and acoustic negative refraction based on a defect-free phoxonic crystal within a triangular lattice. The phoxonic negative refraction is achieved based on abnormal dispersion effect, by intentionally creating convex equal-frequency contours for both photonic and phononic modes. As a potential application, negative refraction imaging for both photonic and phononic modes is also achieved. Numerical simulations based on the finite element method demonstrate the coexistence of negative refraction and the resultant imaging for electromagnetic and acoustic waves. Compared with the defect-based bandgap effects that need low fault tolerance, phoxonic negative refraction relying on passbands has considerable advantages in realizing controllable propagation of waves. The new scheme for the simultaneous control of electromagnetic and acoustic waves provides a potential platform for designing novel phoxonic devices.

Keywords: negative refraction; phoxonic crystals; imaging

Citation: Zhao, S.; Lei, L.; Tang, Q.; Xin, F.; Yu, T. Dual Optical and Acoustic Negative Refraction in Phoxonic Crystals. *Photonics* **2022**, *9*, 908. https://doi.org/10.3390/photonics9120908

Received: 29 October 2022
Accepted: 25 November 2022
Published: 28 November 2022

1. Introduction

The synchronous control of electromagnetic (EM) and acoustic waves has recently attracted considerable attention in periodic structures due to the existence of dual photonic and phononic bandgaps, phoxonic bandgaps [1–4]. The dual bandgaps come from phoxonic crystals (PxCs) [5,6], or optomechanical crystals [7–9], in which materials with optical and acoustic parameters are periodically patterned. PxCs have shown great value for phoxonic sensing [10,11], enhanced photomechanical effects [12–15], slab lenses [16–18], superprism [19], as well as the very recent topological phoxonic waveguides that possess the ability of simultaneous guidance of EM and acoustic waves [20–22].

Apart from the interest in bandgaps [23], particularly, a new mechanism depending on passbands instead of bandgaps for the control of waves has attracted extensive attention of scholars [24,25]. The passbands can give rise to various fantastic transmission phenomena, including negative refraction [26,27], zero refraction [28,29] and self-collimation [24]. Among them, negative refraction has attracted much attention due to their potential applications in focusing, perfect lens, high directivity antenna, electromagnetic cloak, and so on [30,31], since the concept of negative refraction materials was put forward in 1968 by Veselago [32]. Negative refraction means that the incident waves and the refracted waves are on the same side of the normal direction of the interface between two kinds of medium. Compared with the defect-based bandgap effects that need low fault tolerance, negative refraction relying on passbands has considerable advantages in realizing controllable special wave propagation [19]. However, past researches mainly focused on the achievement of the negative refraction depending on either electromagnetic (EM) waves or acoustic waves seperately [33,34]. The existence of photonic negative refractive does not necessarily suggest that the phononic negative refractive can be simultaneously existed, and vice versa. Synchronous negative refraction will enable multi-mode and multi-frequency synchronous control of sound and light, if appropriate materials are used. Such phoxonic refractive

index also provides precise and sensitive optical measurements of mechanical vibrations and a potential platform to study the opto-acoustic interaction.

On this basis, herein, we firstly achieve the negative refraction of the electromagnetic and acoustic waves at the same time, based on a PxC within a triangular lattice. Simultaneous negative refraction effects are further numerically demonstrated. As a potential application, negative refraction imaging for both photonic and phononic modes is also obtained. Our work provides a new scheme to synchronously manipulate photons and phonons, and has potential application in novel phoxonic devices.

2. Principle and Structure Design

Figure 1a shows the schematic diagram of negative refraction, where α is the incident angle in air and the normal of the input interface is along the Γ M direction. The green and black arrows denote the group velocities of the wave in air and PxC, respectively, and the red arrow is the wave vector for both EM and acoustic waves in the PXC. In isotropic homogeneous media, the directions of the wave vector and the group velocity $\vec{v}_g = \nabla_k \omega$ are the same but they are opposite in the negative index medium. Of note, only the negative group velocity resulting from the case that frequencies of the equifrequency contours (EFCs) decrease gradually outward from the center of the Brillouin zone (BZ) could give the opposite direction to the wave vector [35–37], as the wave vector starts from the Γ point with a positive value. The corresponding EFCs in the BZ is thus convex with higher frequencies near the center of the BZ and lower frequencies close to the boundary of the BZ. To achieve the simultaneous convex EFCs and the resultant simultaneous negative refraction, the designed PxC structure is shown in Figure 1b within a triangular lattice, which is composed of silicon dielectric rods, with air as the base. The rod radius r is 0.4a, and a is the lattice constant. Considering practical applications, a is set to be 461 nm, making the desired wavelength of electromagnetic waves locating in the communication band. The material parameters of silicon are as follows: relative dielectric constant of 12, density ρ of 2331 kg/m^3, and sound speed v of 5360 m/s. In our calculation, the band structures and the numerical simulations are based on the finite element method.

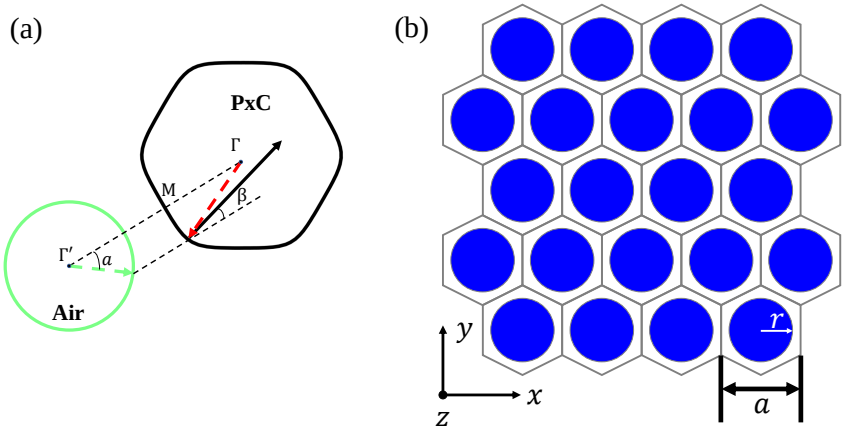

Figure 1. (**a**) Schematic diagram of negative refraction for both EM and acoustic waves in PxC, where green and black lines are EFCs for the same frequency in the air and PxC, respectively. The green arrow represents direction of incident waves and the black arrow denotes the direction of waves in the PxC. The red arrow is wave vector in the PxC. (**b**) Triangular lattice PxC with r being the radius of the Si rod and a being the lattice constant.

3. Dual Optical and Acoustic Negative Refraction Based on 2D PxC

For the realization of negative refraction, the first step is to analyze the band structure of the PxC. Photonic modes are considered first, and we plot its band structure in Figure 2a, with transverse-electric (TE) and transverse-magnetic (TM) modes colored in blue and red, respectively.The definitions for the TE and TM modes are: TE mode has an H field parallel

to the rods, while the TM mode has an E field parallel to the rods. The frequency ranges of the second bands for the two modes are 0.30(c/a)∼0.35(c/a) and 0.22(c/a)∼0.35(c/a) with c being the light speed, respectively. As can be seen, the second bands for the two modes show a negative group velocity and positive wave vector k along the ΓM and ΓK directions, which gives the possibility of negative refraction effect. Further, we plot their EFCs with blue and red solid lines denoting the normalized frequencies 0.3263(c/a) (193.55 THz) and 0.2974(c/a) (212.2 THz) for the TE and TM modes, as shown in Figure 2b,c, respectively. The green dotted lines represent the first Brillouin zone (BZ), and the high symmetric points Γ, M and K are labelled. The locations of the two selected frequencies are indicated by the colored dot-lines in Figure 2a. We further label another two frequencies, one close to the boundary of the BZ, and the another one near the center of the BZ. As can be seen, for the TE modes, the frequency near the boundary of the BZ is 0.3228(c/a) and the frequency near the center of the BZ rises to 0.3362(c/a). Similarly, for the TM modes, the frequency 0.2596(c/a) near the boundary of the BZ is lower than the frequency 0.3209(c/a) near the center of the BZ. One can find that the frequency decreases from the center of the BZ for both the two EM modes, which is the precondition of negative refraction effect, and thus the negative refraction can be expected. To verify this, we simulate the light propagation through the PxC having 9 layers of rods along the ΓM direction with the selected normalized frequencies 0.3263(c/a) and 0.2974(c/a) for the TE and TM modes, as shown in Figure 2d,e, respectively. We can see that when the EM waves for both TE and TM polarizations are incident from the air to the PxC, refracted waves and incident waves appear on the right side of the normal at the same time, and when the EM waves exit from the PxC to the air, refracted waves and incident waves are both on the left side of the normal. Obviously, the phenomenon of refracted waves and incident waves emerging on the same side of the normal is a typical effect of negative refraction.

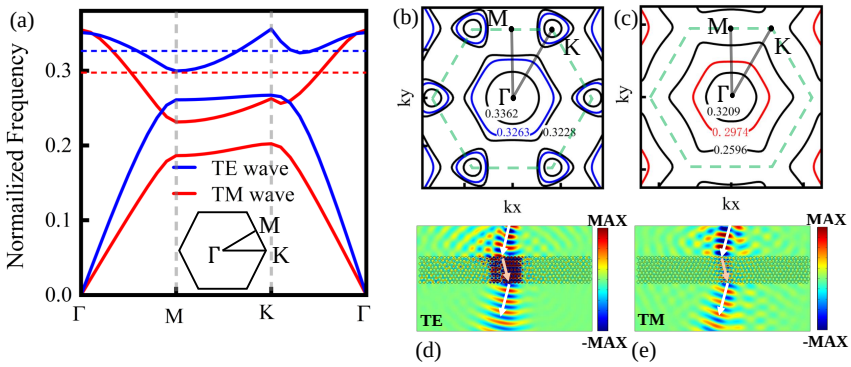

Figure 2. (**a**) Photonic band structure of the PxC with silicon rods in air, with TM and TE modes denoted by the red and blue lines, respectively. The red and blue dashed lines correspond to the normalized frequencies of 0.3263(c/a) and 0.2974(c/a). EFCs of the second band for (**b**) TE and (**c**) TM modes. (**d**) Negative refraction of the TE mode at the frequency of 0.3263(c/a). (**e**) Negative refraction of the TM mode at the frequency of 0.2974(c/a).

For acoustic waves, the band structure is plotted in Figure 3a, and similarly, the second band shows the negative group velocity and positive wave vector along ΓM and ΓK directions. Figure 3b shows the EFCs, and the operating frequency with a value of 0.6927(v/a) (515.4 MHz) is denoted by the orange dashed line. A higher frequency 0.7728(v/a) is close to the center of the BZ, and a lower frequency with a value of 0.6328(v/a) is near the boundary of the BZ. Obviously, frequencies decrease gradually away from the center of BZ, which also foretells the effect of phonoic negative refraction. Next, we simulate the transmission behavior of the acoustic waves passing through the PxC from air, with the frequency 0.6927(v/a). Acoustic waves are incident from the top right of the PxC, and the refracted waves propagate to the bottom right of the PxC. Both incident and refracted acoustic waves appear on the right side of the normal direction of the air-PxC interface.

The situation is similar when acoustic waves enter air from the PxC, but they are all on the left side of the normal direction of the air-PxC interface. Thus, obvious negative refraction can also be observed for the acoustic waves, as shown in Figure 3c. As a result, we achieve the negative refraction for both EM and acoustic waves, relying the second bands that show the convex EFCs based on the same crystal structure.

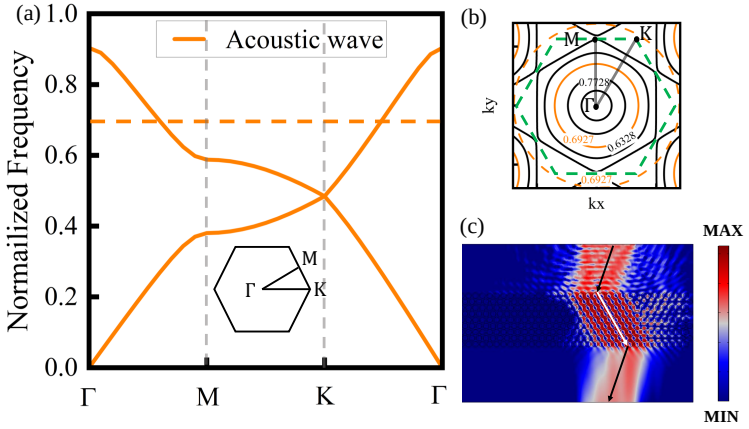

Figure 3. (**a**) Phononic band structure of the PxC, with the orange solid and dashed lines corresponding to the normalized frequency of 0.6927(v/a) in PxC and air, respectively. (**b**) EFCs of the second band. The orange contours represent the frequency of 0.6927(v/a). (**c**) Acoustic negative refraction at the frequency of 0.6927(v/a).

Next, we would like to discuss the dependence of negative refraction on incidence angle. To do this, we investigate the relationship between the refraction angle and the incident angle in Figure 4 for both the photonic and phononic modes. For the TE modes at the normalized frequency 0.3263(c/a), when the incidence angle α increases from 0° to 90°, the refraction angle β increases from 0° to 88°, as the blue line indicates. Note that the EFCs of the TE mode retain a hexagonal feature [see Figure 2b], and this is different from the EFCs of the TM modes that shows a more circular and isotropic feature [see Figure 2c]. The red solid line represents the β-α relationship of TM mode at the normalized frequency 0.2974(c/a). As can be seen, when the incidence angle α increases from 0° to 90°, the refraction angle increases approximately linearly from 0° to 81°. This is because that the EFC of the frequency 0.2974(c/a) of TM modes shown in Figure 2c is closer to the center of BZ than that the EFC of the frequency 0.3263(c/a) of TE modes shown in Figure 2b. Although the refractive index ratio $n_p = n_{air} sin\alpha / sin\beta$ of the TE mode is closer to -1 when incident angle α is close to 90°, its curve is not linear as a whole, so the imaging effect of the TE modes is slightly inferior to that of the TM modes, as also will be demonstrated in Figure 5 in the next section. For acoustic waves, since the radius of the EFC of the frequency 0.6927(v/a) in the PXC is smaller than that of the EFC in the air, there are no refraction waves in the PxC when the incidence angle α is greater than 45°. This is because when acoustic waves are incident from the air into PxC, $k_{||}$ (the tangential component of the wave vector k) should be conserved. The closer the EFC gets to the center of the Brillouin zone, the smaller $k_{||}$ would be in the PxC. This causes range of refraction angles smaller. Nevertheless, the acoustic EFC of this frequency 0.6927(v/a) in the PxC is very close to a circle that shows the isotropic characteristic, as shown in Figure 3b. Hence, the direction of refracted acoustic waves at this frequency will smoothly change with the change of incident angle α, and the convergence effect is also expected. As a result, negative refraction for EM waves of both TM and TE polarizations can be realized in an arbitrary incident angle, that is, the all-angle negative refraction (AANR), while for acoustic waves the negative refraction can only occur within a range of less than or equal to 45°.

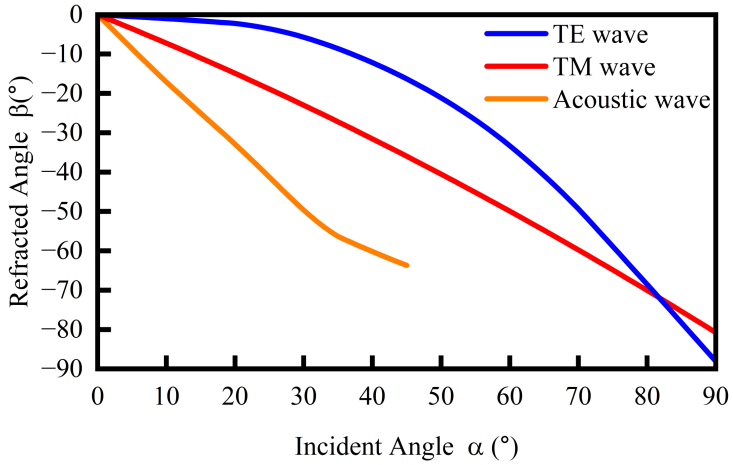

Figure 4. Dependence of refraction angle β on incident angle α.

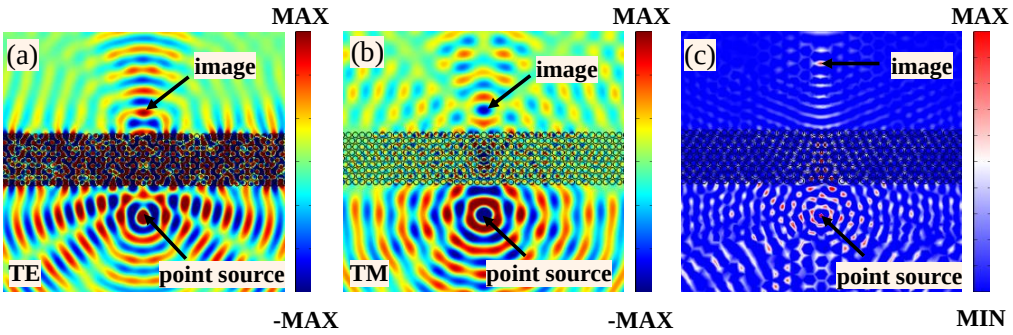

Figure 5. Slab-lens made of the PxC composed of 9 layers of silicon rods arranged in a triangular lattice and placed in air, based on which the imaging of TE, TM and acoustic modes can be achieved. The CW point source is located at the position below the lens with a distance of 5a, and the imaging point is formed above the upper side of the slab-lens. (**a**) Hz field patterns at the frequency of 0.3263(c/a) for TE mode. (**b**) Ez field patterns at the frequency of 0.2974(c/a) for TM mode. (**c**) The pressure field patterns at the frequency of 0.6927(v/a) for acoustic mode.

4. Dual Optical and Acoustic Imaging

Based on the previous analysis of PxC bands and EFCs, we have been able to predict the coexistence of photonic and phononic imaging. It has been a trend to adjust the energy band and EFCs of PxC by adjusting its structure. A 9-layer PxC slab-lens consisting of 100 units per layer is constructed, and the interface normal is along the direction. The continuous wave (CW) point source is placed at a distance 5a below the PxC slab. To avoid reflection interference, absorbing boundary conditions are set around the four sides of the simulation area. Figure 5a depicts a CW magnetic field snapshot, and an image can be found at the position 3.9a above the PxC slab. Although there is a small difference, the simulation results still show a good effect of the slab-lens and the reason is that the refractive index is close to -1. Figure 5b shows a CW electric field snapshot, where an image is observed at a distance 3.4a above the slab. The β-α relationship is similar with each other for TE and TM modes, so the location of the images of the two modes are also close. Figure 5c shows the pressure field distribution for the acoustic mode. The image appears at 10a above the slab. Of note, the image of the acoustic modes has a more pronounced distortion and the imaging focus contains some elongation compared with the photonic modes. This is mainly because the incident angle range of the acoustic modes allowed by negative refraction is relatively small compared with the photonic modes.By comparing with the three images of the TE, TM, and acoustic modes, we can find that they share distinct characteristics due to the distinct β-α relationship. Specially, the negative refraction of the acoustic mode allows the smallest range of incidence angle α, so its image is

significantly elongated and the results are the least effective. TE mode has reached AANR, but due to its low degree of linearity, the image generated has certain distortion. The β-α relationship of the TM mode is closest to the linear tangent of -1, and hence its imaging effect is the best among the three modes.

In addition, we further measure the distribution of the intensity of the images in Figure 6. The full width at half maximum (FWHM) of the images for TE, TM, and acoustic modes are 2.65a, 1.48a, and 0.5a, respectively, which are smaller than their corresponding wavelengths.

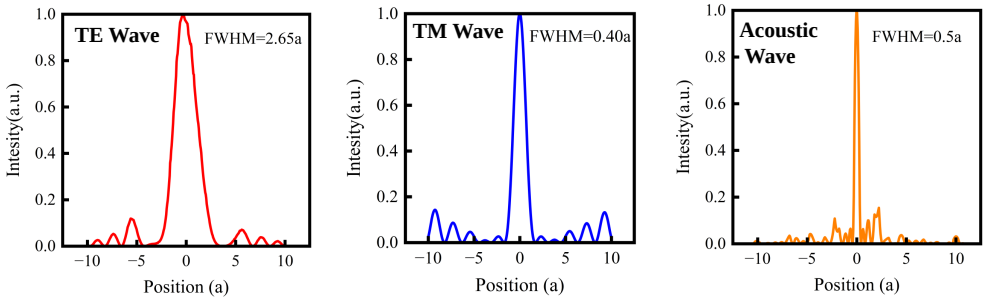

Figure 6. Intensity distributions of images in the cross-section along the x direction for (**a**) TE mode, (**b**) TM mode, and (**c**) acoustic mode. FWHMs for the three modes are 2.65a, 1.48a, and 0.5a, respectively.

5. Conclusions

In conclusion, simultaneous negative refraction and the resultant imaging for both EM and acoustic waves are realized based on a PxC of triangular lattice, which are numerically demonstrated by finite element method. By choosing appropriate geometric parameters, the precondition for the effect of negative refraction, the convex EFCs, can be obtained for both the photonic and phononic modes. In practice, transmission loss caused by the defects and backscattering and the out-of-plane radiation loss have a considerable impact on transmission efficiency. These can be alleviated to some extent by the bound states in continuum (BIC) and topology in photonic/phononic crystals [38,39]. The achievement of simultaneous negative refraction via the PxC demonstrates a new way for simultaneously guiding light and sound transmission based on defect-free structures, which can also be extended to other kinds of PxCs within different lattices.

Author Contributions: Conceptualization, T.Y.; methodology, software, and validation, S.Z.; formal analysis, investigation, resources, L.L.; data curation, Q.T. and F.X.; writing—original draft preparation, S.Z.; writing—review and editing, T.Y.; visualization, T.Y.; supervision, T.Y.; project administration, T.Y.; funding acquisition, T.Y. All authors have read and agreed to the published version of the manuscript.

Funding: National Natural Science Foundation of China (12064025); Natural Science Foundation of Jiangxi Province (20212ACB202006,20202BABL201021); Major Discipline Academic and Technical Leaders Training Program of Jiangxi Province (20204BCJ22012).

Institutional Review Board Statement: Not applicable.

Informed Consent Statement: Not applicable.

Data Availability Statement: Not applicable.

Conflicts of Interest: The authors declare no conflict of interest.

References

1. Schneider, D.; Liaqat, F.; Boudouti, E.H.E.; Abouti, O.E.; Tremel, W.; Butt, H.J.; Djafari-Rouhani, B.; Fytas, G. Defect-Controlled Hypersound Propagation in Hybrid Superlattices. *Phys. Rev. Lett.* **2013**, *111*, 164301. [CrossRef] [PubMed]
2. Alonso-Redondo, E.; Huesmann, H.; El Boudouti, E.H.; Tremel, W.; Djafari-Rouhani, B.; Butt, H.J.; Fytas, G. Phoxonic Hybrid Superlattice. *ACS Appl. Mater. Interfaces* **2015**, *7*, 12488–12495. [CrossRef] [PubMed]
3. Li, H.; Liu, W.; Yu, T.; Wang, T.; Liao, Q. Simultaneous unidirectional reciprocal filters of electromagnetic and elastic waves based on the modal symmetry of phoxonic crystal waveguides and cavity. *Phys. Lett. A* **2020**, *384*, 126499. [CrossRef]
4. Alagoz, S.; Alagoz, B.B.; Sahin, A.; Nur, S. Negative refractions by triangular lattice sonic crystals in partial band gaps. *Chin. Phys. B* **2015**, *24*, 046201. [CrossRef]
5. El-Jallal, S.; Oudich, M.; Pennec, Y.; Djafari-Rouhani, B.; Makhoute, A.; Gomis-Bresco, J.; Navarro-Urrios, D.; Martínez, A.; Torres, C.M.S. Cavity modes and optomechanic interactions in strip waveguide. *IOP Conf. Ser. Mater. Sci. Eng.* **2014**, *68*, 012003. [CrossRef]
6. Ma, X.; Xiang, H.; Yang, X.; Xiang, J. Dual band gaps optimization for a two-dimensional phoxonic crystal. *Phys. Lett. A* **2021**, *391*, 127137. [CrossRef]
7. Eichenfield, M.; Chan, J.; Camacho, R.M.; Vahala, K.J.; Painter, O. Optomechanical crystals. *Nature* **2009**, *462*, 78–82. [CrossRef]
8. Liu, S.; Tong, H.; Fang, K. Optomechanical crystal with bound states in the continuum. *Nat. Commun.* **2022**, *13*, 3187. [CrossRef] [PubMed]
9. Burek, M.J.; Cohen, J.D.; Meenehan, S.M.; El-Sawah, N.; Chia, C.; Ruelle, T.; Meesala, S.; Rochman, J.; Atikian, H.A.; Markham, M.; et al. Diamond optomechanical crystals. *Optica* **2016**, *3*, 1404. [CrossRef]
10. Sharma, G.; Kumar, S.; Singh, V. Design of Si–SiO_2 phoxonic crystal having defect layer for simultaneous sensing of biodiesel in a binary mixture of diesel through optical and acoustic waves. *Acoust. Phys.* **2017**, *63*, 159–167. [CrossRef]
11. Li, K.Y.; Sun, X.W.; Song, T.; Wen, X.D.; Wang, Y.W.; Liu, X.X.; Liu, Z.J. A high-sensitivity liquid concentration-sensing structure based on a phoxonic crystal slot nanobeam. *J. Appl. Phys.* **2022**, *131*, 024501. [CrossRef]
12. Ma, T.X.; Wang, Y.S.; Zhang, C.; Su, X.X. Simultaneous guiding of slow elastic and light waves in three-dimensional topology-type phoxonic crystals with a line defect. *J. Opt.* **2014**, *16*, 085002. [CrossRef]
13. Schmidt, M.; Kessler, S.; Peano, V.; Painter, O.; Marquardt, F. Optomechanical creation of magnetic fields for photons on a lattice. *Optica* **2015**, *2*, 635. [CrossRef]
14. Aram, M.H.; Khorasani, S. Optomechanical coupling strength in various triangular phoxonic crystal slab cavities. *J. Opt. Soc. Am. B* **2018**, *35*, 1390. [CrossRef]
15. Wang, D.H.; Lee, K.M.; Lee, D.H.; Baczkowski, M.; Lee, J.G.; Wie, J.J.; Tan, L.S. Intermolecular Interactions and Intramolecular Motions in Photomechanical Effect: Nonlinear Thermo- and Photomechanical Behaviors of Azobenzene-Functionalized Amide–Imide Block Copolymers. *ACS Appl. Mater. Interfaces* **2021**, *13*, 48127–48140. [CrossRef]
16. Pendry, J.B. Negative Refraction Makes a Perfect Lens. *Phys. Rev. Lett.* **2000**, *85*, 3966–3969. . [CrossRef] [PubMed]
17. Feng, S.; Li, Z.Y.; Feng, Z.F.; Cheng, B.Y.; Zhang, D.Z. Engineering the imaging properties of a metallic photonic-crystal slab lens. *Appl. Phys. Lett.* **2006**, *88*, 031104. [CrossRef]
18. Cai, Z.; Zhao, S.; Huang, Z.; Li, Z.; Su, M.; Zhang, Z.; Zhao, Z.; Song, Y. Negative Refraction Acoustic Lens Based on Elastic Shell Encapsulated Bubbles. *Adv. Mater. Technol.* **2022**, *7*, 2101186. [CrossRef]
19. Kosaka, H.; Kawashima, T.; Tomita, A.; Notomi, M.; Tamamura, T.; Sato, T.; Kawakami, S. Superprism phenomena in photonic crystals: Toward microscale lightwave circuits. *J. Light. Technol.* **1999**, *17*, 2032–2038. [CrossRef]
20. Ma, T.X.; Zhang, C.; Wang, Y.S. Topological electromagnetic and elastic states in phoxonic crystal cavity arrays. *PAMM* **2021**, *20*. [CrossRef]
21. Xia, B.; Fan, H.; Liu, T. Topologically protected edge states of phoxonic crystals. *Int. J. Mech. Sci.* **2019**, *155*, 197–205. [CrossRef]
22. Hu, Z.; Lei, L.; He, L.; Liu, W.; Yu, T.; Wang, T.; Liao, Q. Simultaneous photonic and phononic topological pseudospin-dependent edge states in phoxonic crystals. *Europhys. Lett.* **2022**, *138*, 15001. [CrossRef]
23. Wu, F.; Lyu, K.; Hu, S.; Yao, M.; Xiao, S. Ultra-large omnidirectional photonic band gaps in one-dimensional ternary photonic crystals composed of plasma, dielectric and hyperbolic metamaterial. *Opt. Mater.* **2021**, *111*, 110680. . [CrossRef]
24. Tan, Y.; Yu, T.; Yu, M.; Liu, W.; Wang, T.; Liu, N.; Liao, Q. Simultaneous beam guides of electromagnetic and acoustic waves in defect-free phoxonic crystals using self-collimation effect. *Appl. Phys. Express* **2019**, *12*, 062015. [CrossRef]
25. Xiao, S.; Liu, T.; Wang, X.; Liu, X.; Zhou, C. Tailoring the absorption bandwidth of graphene at critical coupling. *Phys. Rev. B* **2020**, *102*, 085410. [CrossRef]
26. Morvan, B.; Tinel, A.; Hladky-Hennion, A.C.; Vasseur, J.; Dubus, B. Experimental demonstration of the negative refraction of a transverse elastic wave in a two-dimensional solid phononic crystal. *Appl. Phys. Lett.* **2010**, *96*, 101905. [CrossRef]
27. Nemat-Nasser, S. Unified homogenization of photonic/phononic crystals with first-band negative refraction. *Mech. Mater.* **2017**, *105*, 29–41. [CrossRef]
28. Li, Y.; Jiang, H.T.; Liu, W.W.; Ran, J.; Lai, Y.; Chen, H. Experimental realization of subwavelength flux manipulation in anisotropic near-zero index metamaterials. *EPL Europhys. Lett.* **2016**, *113*, 57006. [CrossRef]
29. Lei, L.; Yu, T.; Liu, W.; Wang, T.; Liao, Q. Dirac cones with zero refractive indices in phoxonic crystals. *Opt. Express* **2021**, *30*, 308. [CrossRef]

30. Kong, J. Electromagnetic Wave Interaction With Stratified Negative Isotropic Media—Abstract. *J. Electromagn. Waves Appl.* **2001**, *15*, 1319–1320. [CrossRef]
31. Hannan, S.; Islam, M.T.; Soliman, M.S.; Sahar, N.B.M.; Singh, M.S.J.; Faruque, M.R.I.; Alzamil, A. A filling-factor engineered, perfect metamaterial absorber for multiple applications at frequencies set by IEEE in C and X bands. *J. Mater. Res. Technol.* **2022**, *19*, 934–946. [CrossRef]
32. Veselago, V.G. The electrodynamics of substances with simultaneously negative values of ε and μ. *Sov. Phys. Uspekhi* **1968**, *10*, 509–514. [CrossRef]
33. Liu, Y.; Wang, G.P.; Pendry, J.B.; Zhang, S. All-angle reflectionless negative refraction with ideal photonic Weyl metamaterials. *Light. Sci. Appl.* **2022**, *11*, 276. [CrossRef] [PubMed]
34. Nemat-Nasser, S. Inherent negative refraction on acoustic branch of two dimensional phononic crystals. *Mech. Mater.* **2019**, *132*, 1–8. [CrossRef]
35. Lu, M.H.; Zhang, C.; Feng, L.; Zhao, J.; Chen, Y.F.; Mao, Y.W.; Zi, J.; Zhu, Y.Y.; Zhu, S.N.; Ming, N.B. Negative birefraction of acoustic waves in a sonic crystal. *Nat. Mater.* **2007**, *6*, 744–748. [CrossRef]
36. Ummer, K.V.; Vijaya, R. All-angle negative refraction effects and subwavelength imaging in photonic crystals with honeycomb lattice. *J. Nanophotonics* **2017**, *11*, 036005. [CrossRef]
37. Jiang, L.; Wu, H.; Li, X. Dual-negative-refraction and imaging effects in normal two-dimensional photonic crystals with hexagonal lattices. *Opt. Lett.* **2012**, *37*, 1829. [CrossRef] [PubMed]
38. Zhang, Z.; Qin, F.; Xu, Y.; Fu, S.; Wang, Y.; Qin, Y. Negative refraction mediated by bound states in the continuum. *Photonics Res.* **2021**, *9*, 1592. [CrossRef]
39. Huang, H.; Huo, S.; Chen, J. Subwavelength elastic topological negative refraction in ternary locally resonant phononic crystals. *Int. J. Mech. Sci.* **2021**, *198*, 106391. [CrossRef]